Enhanced spin Hall response from aligned Kramers-Weyl points in high Chern number semimetals

C. O. Ascencio, Wei Jiang, ** D. J. P. de Sousa, Seungjun Lee, Jian-Ping Wang, 1,2 and Tony Low 1,2,†

School of Physics and Astronomy, University of Minnesota, Minneapolis, Minnesota 55455, USA

Department of Electrical and Computer Engineering, University of Minnesota, Minneapolis, Minnesota 55455, USA

(Received 25 July 2023; accepted 26 October 2023; published 29 November 2023)

We propose a spin Hall effect (SHE) enhancement mechanism due to Kramers-Weyl point (KWP) alignment in chiral topological semimetals with high Chern numbers. Through model Hamiltonian calculations, we identify enhancements in the intrinsic spin Hall conductivity (SHC) and the spin Hall angle (SHA). Such enhancements, attributed to a unique high Chern number KWP energetic alignment and a high degree of band nesting induced by spin-orbit coupling, strongly depend on orbital-orbital interactions. This represents a mechanism to enhance SHE, differing from the spin-orbit induced anticrossing mechanism in gapped systems. Guided by this principle, we corroborate our results by means of first-principles calculations and reveal multiple realistic materials with large intrinsic SHCs and even larger SHAs than Pt.

DOI: 10.1103/PhysRevB.108.L201404

Introduction. The efficient generation of spin currents is a highly sought-after goal within the spintronics community [1–20]. Of particular interest is the intrinsic spin Hall effect (SHE), which relies on the spin-orbit coupling (SOC) of a material, independent of any impurity scattering mechanisms [15,21–23]. An anomalous velocity due to the non-Abelian Berry curvature associated with a material's band structure is the source of the intrinsic SHE [15,21–26]. To date, the mechanism to enhance the intrinsic spin Hall conductivity (SHC) has been primarily attributed to SOC-induced anticrossings [10,27–29] and no general theory to enhance the spin Hall angle (SHA) has been developed.

Analogous to the anomalous Hall effect (AHE) in magnetic systems, where a larger AHE can be achieved in topological systems with higher Chern numbers [30–32], high Chern numbers in nonmagnetic materials may lead to enhanced SHCs [33–35]. Chiral topological semimetals are known to host Kramers-Weyl points (KWPs) with the largest possible Chern number [36], C = 4 [35,37,38], which are suggested to support the longest possible Fermi arc surface states, quantized photogalvanic currents, a unique longitudinal magnetoelectric effect, among other exotic phenomena [37–45].

Previous intrinsic SHE studies on topological materials mainly examined gapped systems with $\mathcal{C}=1$, where SOC-induced gaps are responsible for the large SHC [10,29,46–49]. The SHC in chiral topological semimetals is fundamentally different due to their gapless nature and variable Chern numbers associated with KWPs [35,36,50,51]. Additionally, due to their relatively low charge conductivity, semimetals with appreciable SHCs may lead to large SHAs. Chiral topological semimetals, therefore, provide an ideal material platform to reveal potentially novel SHE physics in high Chern number semimetallic systems and to search for highly efficient spin

In this Letter, we propose a distinctive intrinsic SHE enhancement mechanism in high Chern number chiral topological semimetals and predict promising material candidates with large SHE. We first uncover positive correlations between the SHC/SHA and Chern number using multiorbital chiral semimetal toy models with tunable orbital degeneracy and orbital-orbital coupling, where the large spin Berry curvature (SBC) near KWPs of the highest Chern number is the main source of the SHC. Such a SHE enhancement can be ascribed to energetic alignments between KWPs via tunable orbital-orbital coupling. We corroborate our findings by means of a space group 198 (SG-198) tight-binding model carrying C = 4, where SOC-induced nesting between linearly dispersing bands that emanate from C = 4 KWPs leads to significant SHE (SHC and SHA) enhancement at alignment. This is further supported by first-principles calculations involving 37 gapless C = 4 materials from the same space group. In particular, two of these materials, BiTePd and BiPdSe, exhibit two of the largest SHAs, surpassing that of Pt, reproducing the salient characteristic features of our SG-198 model. Our study reveals a mechanism for SHE enhancement associated with energetically aligned pointlike topological band crossings and provides a clear strategy for the use of high Chern number semimetals for energy efficient spintronics.

Chiral semimetal toy models. We begin by considering a time-reversal (\mathcal{T}) symmetric, single-orbital, chiral semimetal model with $\mathcal{C}=1$ KWPs, which describes crystalline systems from SG-16 [35]. The nearest-neighbor (NN) tight-binding Hamiltonian can be expressed as

$$\mathcal{H} = \sum_{i=1}^{3} \left[t_s^i \cos(k_i) \sigma_0 + t_{SO}^i \sin(k_i) \sigma_i \right], \tag{1}$$

where the first three terms are NN hoppings, t_s^i , i = 1-3 denoting the hopping amplitude along x, y, and z directions.

sources for applications in magnetic based memories and inmemory computing technologies [18,52–55].

^{*}tj.jwei@gmail.com

[†]tlow@umn.edu

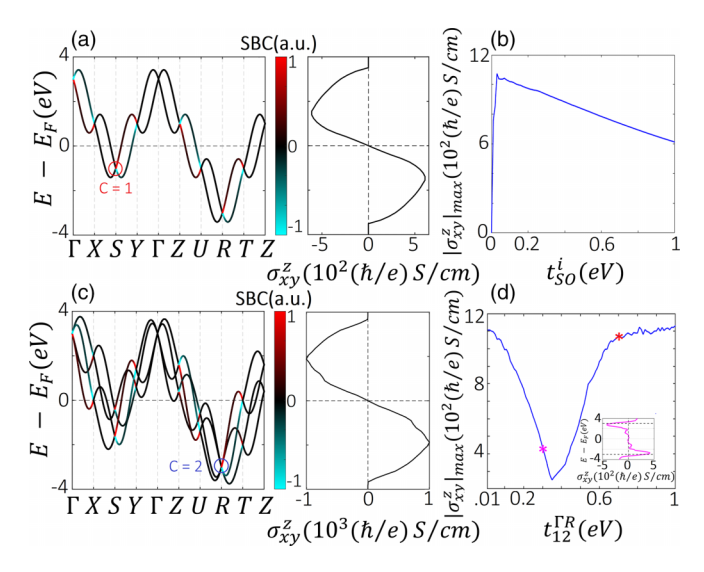


FIG. 1. The energy spectrum and SHC for chiral semimetal models. (a) $\mathcal{C}=1$ model band structure with SBC distribution and SHC. Red circle indicates a $\mathcal{C}=1$ KWP. (b) The effect of SOC on the maximum SHC [56]. (c) Same as (a) for $\mathcal{C}=2$ model ($t_{12}^{\Gamma R}=0.1\,\mathrm{eV}$). Blue circle indicates a $\mathcal{C}=2$ KWP. (d) The effect of orbital-orbital coupling on the maximum SHC. The inset shows that the SHC peaks at the energies near the $\mathcal{C}=2$ KWP positions (dashed black lines) for $t_{12}^{\Gamma R}=0.3\,\mathrm{eV}$ (magenta asterisk). Red asterisk corresponds to alignment of high Chern number KWPs with a subset of $\mathcal{C}=1$ KWPs at $t_{12}^{\Gamma R}=0.67\,\mathrm{eV}$ [56].

The following three terms are SOC components that define the chirality with SOC strengths t_{SO}^i [35]. The Pauli matrices σ_i operate on the spin space. SOC lifts the spin-degeneracy throughout the Brillouin zone (BZ) except at time-reversal invariant momenta (TRIM), as enforced by Kramer's theorem, which results in KWPs with $\mathcal{C} = 1$ [Fig. 1(a)] [35,56].

We calculate the energy-dependent SHC based on the Kubo formula that integrates the SBC of the occupied bands throughout the BZ [15,23,25,28,57]. The maximum SHC with the selected hoppings is about $|\sigma_{xy}^z| \sim 610(\hbar/e)$ S/cm [Fig. 1(a)] [56]. The SBC distribution shown in Fig. 1(a) reveals that the main contribution to the SHC comes from bands near the KWPs [56]. We also studied the influence of SOC on the SHC and plotted the maximum SHC as a function of SOC strength [Fig. 1(b)]. We observe a peak SHC at low SOC followed by a monotonic decrease at larger SOCs due to further SOC-induced band splitting [56,58].

To understand the correlation between the SHC and Chern number in semimetallic systems, we build upon Eq. (1) to construct a four-band model that supports KWPs with $\mathcal{C}=2$. We double the orbital degeneracy within the unit cell, which is common in chiral crystals, and incorporate spin-conserving, \mathcal{T} -symmetric, SG-16 symmetric orbital-orbital couplings [56],

$$\mathcal{H} = \begin{bmatrix} H_1 & H_c \\ H_c^{\dagger} & H_2 \end{bmatrix}, \tag{2}$$

with two distinct diagonal blocks $H_{n=1,2} = \sum_{i=1}^{3} [t_{s,n}^{i} \cos(k_{i})\sigma_{0} + t_{SO,n}^{i} \sin(k_{i})\sigma_{i}]$ and one off-diagonal term, H_{c} , which defines the orbital-orbital coupling. For

simplicity, and consistency with the previous model, the orbital-orbital coupling matrix, $H_c = t_{12}^{\Gamma R} [3\cos(k_z) + 2\cos(k_y) - 5\cos(k_x)]I$, is chosen to preserve electron-hole, time-reversal, and SG-16 crystalline symmetries [56], where I is the second-order unit matrix and $t_{12}^{\Gamma R}$ represents the orbital-orbital coupling strength. The form of H_c guarantees C = 2 KWPs at Γ and R [56].

Before turning on orbital-orbital coupling, this model represents a trivial duplication of the two-band model in Eq. (1), which consists of fourfold degenerate points (i.e., two overlapping $\mathcal{C}=1$ KWPs) at all TRIMs [56]. Orbital-orbital coupling energetically separates most of these degeneracies into two $\mathcal{C}=1$ KWPs. Importantly, the fourfold degeneracies at Γ and R are preserved due to the coexistence of orbital degeneracy, \mathcal{T} symmetry, and the form of the orbital-orbital coupling. The calculated energy-dependent SHC [Fig. 1(c)] [56] exhibits a similar trend to the $\mathcal{C}=1$ model. The maximum SHC for SOC strengths comparable to the $\mathcal{C}=1$ case is nearly twice that of the $\mathcal{C}=1$ results [Fig. 1(c)], as expected since the SHC is proportional to the band degeneracy [56].

To investigate the effect of orbital-orbital coupling on the SHC, we plot the maximum possible SHC as a function of orbital-orbital coupling strength, $t_{12}^{\Gamma R}$ [Fig. 1(d)]. Increasing $t_{12}^{\Gamma R}$ initially leads to a decrease in the maximum SHC due to an increase in the energetic misalignment between C=1 KWPs that smears out their SBC contributions [56]. On the other hand, the contribution from energetically fixed KWPs at Γ and R, with C=2 remains almost unchanged with variable $t_{12}^{\Gamma R}$ [see Fig. 1(d) inset, $t_{12}^{\Gamma R}=0.3\,\mathrm{eV}$] [56]. Interestingly, further increase in $t_{12}^{\Gamma R}$ leads to an increase in the SHC [Fig. 1(d)] due to an energetic alignment between KWPs from different TRIMs [56]. A similar analysis with C=2 KWPs at Γ and S, which breaks the electron-hole symmetry, exhibits similar behavior [56].

We further investigate systems with higher Chern numbers, i.e., $\mathcal{C}=3$ and 4, using a six and eight-band model Hamiltonian by increasing the orbital degeneracy to three and four orbitals, respectively [56]. Similar orbital-orbital coupling terms are incorporated while preserving the symmetries of SG 16 to generate higher Chern number systems within the same framework [56]. Further analysis confirms a positive correlation between Chern number and SHC for a significant parameter space of these models [56].

The correlation between SHA and Chern number under variable orbital-orbital coupling is less obvious, since the effect of band degeneracy is factored out. To investigate this, we calculate the difference of SHCs and SHAs at $E_F = 3 \,\mathrm{eV}$ (energy of high Chern number KWP at Γ) between C=2 and C=3 models for $0.01\,\mathrm{eV} \leqslant t_{12}^{\Gamma R} \leqslant 0.5\,\mathrm{eV}$, as displayed in Fig. 2. Interestingly, we find that concurrent positive correlations between Chern number, SHC, and SHA can be achieved for a specific range of orbital-orbital coupling strengths, as highlighted in Fig. 2(a) [56]. To unravel the underlying source of these correlations, we plot the band structures of the C=3model [56] at the SHC difference minimum and maximum [Fig. 2(a) top panel]. The band structure for the maximum difference [Fig. 2(b)] exhibits good alignment between the high Chern number KWP at Γ and two other KWPs (SBC sources) at S and Z, as indicated by the red dashed lines, while the band structure for the minimum difference [Fig. 2(c)] shows

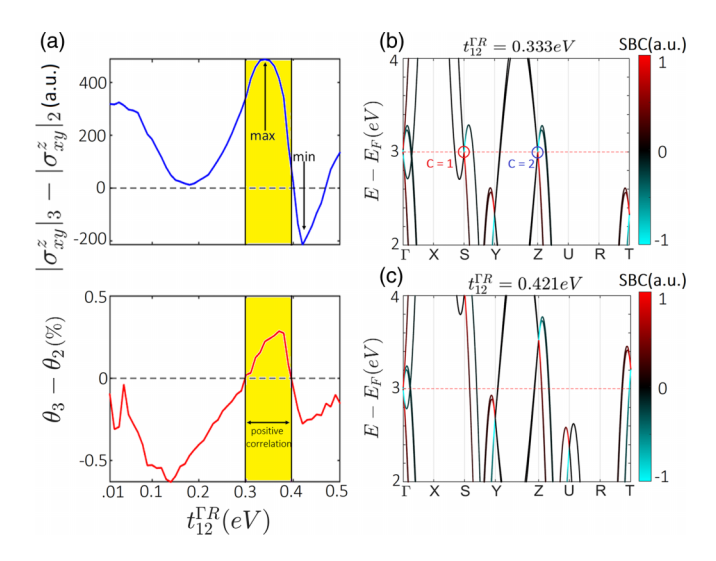


FIG. 2. KWP energetic alignment and Chern number-SHE correlation. (a) Difference in SHCs (upper panel) and SHAs (lower panel) between C=2 and C=3 models for 0.01 eV $\leqslant t_{12}^{\Gamma R} \leqslant 0.5$ eV. (b) and (c) C=3 model band structure with KWP alignment [maximum in (a)] at $t_{12}^{\Gamma R}=0.333$ eV and misalignment [minimum in (a)] at $t_{12}^{\Gamma R}=0.421$ eV, respectively. Range of orbital-orbital coupling strengths that support concurrent positive correlations between Chern number, SHC, and SHA is highlighted.

an obvious energetic misalignment between them. Thus, it is an energetic KWP alignment that leads to constructive contributions to both the SHC and SHA. Similar results are observed between other Chern number systems [56].

These results indicate that gapless higher Chern number systems can concurrently have higher SHCs and SHAs under KWP alignment, which is tunable through orbital-orbital coupling. We note that a trivial increase in the orbital degeneracy in the absence of orbital-orbital coupling would render a nearly constant SHA with variable Chern number [56]. Our models, therefore, hint at the importance of orbital-orbital interactions in determining the SHC and SHA of these distinct Chern number systems, and thus provides a feasible approach for optimizing the SHA in gapless high Chern number materials.

We note that the Hamiltonians used thus far rely critically on the specific form of the orbital-orbital coupling, which is artificial and may not represent realistic material systems. Fortunately, such simple artificial models can be used to describe realistic chiral systems with an appropriate choice of orbital-orbital coupling consistent with the symmetries of a specific chiral space group. We elaborate on this point in the highest Chern number system and demonstrate an enhanced SHC and, more importantly, SHA enhancement with high Chern number KWP alignment.

Chiral semimetal with C=4. Building upon Eq. (1), we construct an eight-band model by quadrupling the orbitals in the system. Rather than artificially placing all the orbitals at the same unit cell position, we evenly distribute them by constructing a face-centered cubic (FCC) unit cell [Fig. 3(a)]. The NN interactions, as described by Eq. (1), become next-nearest neighbor (NNN) interactions, and the orbital-orbital terms describe NN interactions. The effective 8×8 Hamiltonian

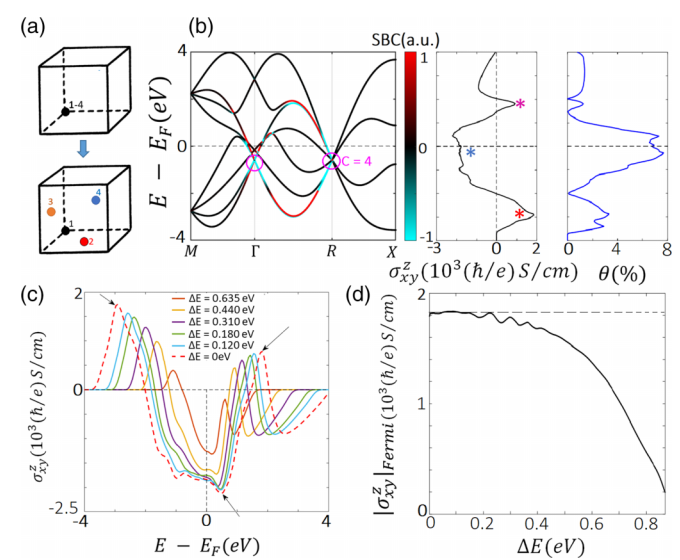


FIG. 3. SHE of $\mathcal{C}=4$ system. (a) Unit cell of SG-16 and SG-198 models. (b) Band structure of SG-198 model at $\mathcal{C}=4$ KWP alignment with SBC distribution, energy-dependent SHC with camel-back structure, and SHA(θ) [56]. Magenta circles indicate $\mathcal{C}=4$ KWPs. Red and magenta asterisks indicate peaks associated with band nesting whereas the blue one indicates a deep valley from large SBC near aligned $\mathcal{C}=4$ KWPs. (c) Evolution of energy-dependent SHC with changes in $\mathcal{C}=4$ KWP separation ($\Delta E=E_{\Gamma}-E_{R}=0$ corresponds to alignment). Arrows indicate enhancements in peaks and deep valleys. (d) Evolution of SHC at $E=E_{F}$ with changes in $\mathcal{C}=4$ KWP separation.

can be written as [56]

$$\mathcal{H} = \epsilon I + H_{\text{NNN}} + H_{\text{NN}} + H_{\text{NNsoc}}, \tag{3}$$

where the first term is an on-site potential and the second describes NNN interactions, as inherited from Eq. (1). The following two terms define NN spin-conserving interactions and NN symmetry-preserving SOCs, respectively (See the SM [56] for more details). We note that, apart from the on-site potential and NNN SOC terms, this model coincides with the one used by Chang *et al.* [37].

The band structure, energy-dependent SHC, and SHA at high Chern number KWP alignment are presented in Fig. 3(b). The spectrum supports a nontrivial fourfold degeneracy at Γ and an eightfold one at R, both of which carry $\mathcal{C} = 4$ [56]. The bands emanating from the C = 4 KWPs contribute sizably to the SHC [59] as displayed by the SBC distribution [Fig. 3(b)], which is a consequence of a combination of the high band degeneracy and SOC-induced band nesting. The energy dependent SHC forms a camel-back type structure [Fig. 3(b) center panel] where two large peaks (red and magenta asterisks) are generated by large, positive SBC contributions from six nested bands which, in part, form the C = 4 KWP at R. The negative SBC energetically near the C = 4 KWPs gives rise to the deep valley in the SHC around $E = E_F$ (blue asterisk). The energy-dependent SHA [Fig. 3(b) right panel] consists of three peaks, two of which coincide with the large peaks in the SHC. The central SHA peak is a consequence of the deep valley in the SHC and the low density of states around $E = E_F$, both of which are a consequence of C = 4

KWP alignment [56]. A comparison of the SHA between appreciably misaligned and aligned C = 4 KWPs reveals that the Fermi level SHA increases by a factor of three at alignment [56].

The influence of $\mathcal{C}=4$ KWP separation ($\Delta E=E_{\Gamma}-E_{R}$), which is tuned via orbital-orbital coupling [56], on the energy-dependent SHC is also studied [Fig. 3(c)]. At large $\mathcal{C}=4$ KWP separation (small orbital-orbital coupling) the band structure is similar to the trivial case where an eightfold band degeneracy exists throughout the BZ [56]. Decreasing ΔE (increasing orbital-orbital coupling) leads to an increase in the SHC magnitude, which is attributed to the constructive SBC contributions from bands emanating from $\mathcal{C}=4$ KWPs. We also examined the evolution of the SHC at $E=E_{F}$ for a larger range of ΔE [Fig. 3(d)] and find that the SHC saturates around alignment. The models studied in this work, therefore, predict SHE (SHC and SHA) enhancement at KWP alignment. We verify this prediction via first principles calculations involving 37 compounds.

SHE of SG-198 chiral topological semimetals. Guided by the preceding principles, we focus on material systems with C = 4, i.e., chiral topological semimetals from SG-198, to identify materials with large SHCs and SHAs. We studied 37 materials within SG 198 with nonmagnetic ground states and the required chiral crystal structure [35,60,61] within the context of density functional theory [56,62–67]. We elaborate in detail on two representatives, BiTePd and BiPdSe (see the SM for 35 additional materials [56]), which fulfill the $\mathcal{C}=4$ KWP alignment criterion described. Their crystal structure has four atoms per element in the unit cell with Bi and Te(Se) forming opposite rotating chains along the [111] direction [Fig. 4(a)]. Their relativistic band structures support a fourfold KWP at Γ and a sixfold KWP at R [Figs. 4(b) and 4(c) left panels], which are protected by the presence of three nonsymmorphic twofold screw axes, a threefold rotation axis, and \mathcal{T} symmetry [37].

The energy-dependent SHCs for an energy window of 2 eV around the Fermi level are shown in the right panels of Figs. 4(b) and 4(c). The Fermi level SHC for BiTePd (BiPdSe) is about $|\sigma_{xy}^z| = 893 (\hbar/e) \text{S/cm}$ ($|\sigma_{xy}^z| =$ $590 (\hbar/e)$ S/cm) [28,56]. Importantly, we observe a characteristic camel-back structure in the SHC similar to the SG-198 model results [Fig. 3(b) center panel] with the corresponding features indicated by colored asterisks for comparison [Figs. 4(b) and 4(c) right panels]. For both representative materials, the large peak at the Fermi level, which is enhanced by KWP alignment (we further corroborate this mechanism via strain engineering [56]), is a consequence of the large SBC contributions from SOC-induced band nesting of six linearly dispersing bands that emanate from the C = 4 KWP at R. Additionally, due to the pointlike nature of the topological band crossings, their alignment, and the large energy gradient of the linearly dispersing bands, the corresponding density of states can be relatively small in comparison to Pt and may lead to larger SHAs.

Finally, the calculated SHAs $(\theta = \frac{2e}{\hbar} \frac{\sigma_{xy}^z}{\sigma_{yy}})$ and SHCs (σ_{xy}^z) for 37 materials from SG 198 (and fcc Pt: $\theta_{Pt} = 0.028$ [56]) at the Fermi level are displayed in Fig. 4(d). Two of the largest possible Fermi level SHAs correspond to our two representative materials (BiTePd: $\theta = 0.063$, and BiPdSe: $\theta = 0.053$).

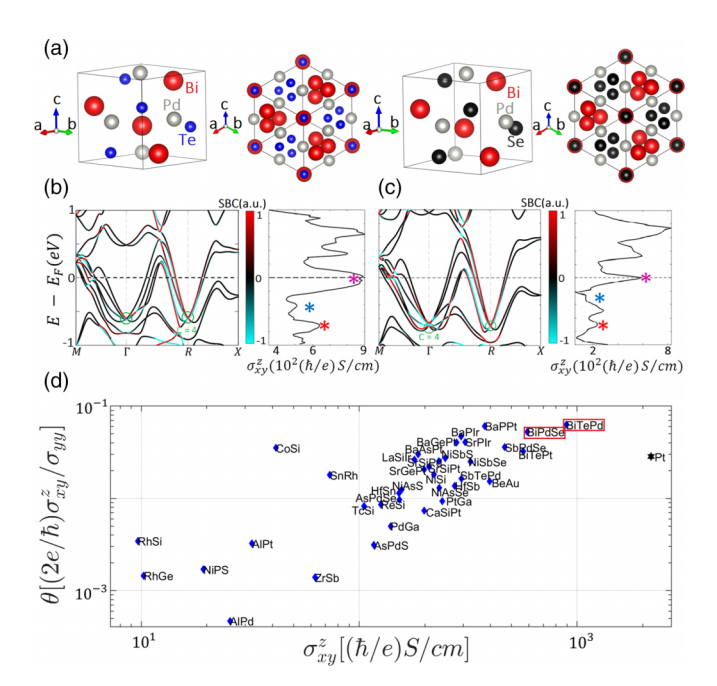


FIG. 4. Crystal structures, band structures, SHCs, and SHAs of SG-198 chiral topological semimetals. (a) Crystal structures of BiTePd and BiPdSe. (b) and (c) Band structure and SHC of BiTePd and BiPdSe, respectively. Colored asterisks correspond to same features in Fig. 3(b) center panel. (d) SHAs (θ), and SHCs of 37 SG-198 materials at Fermi level with representatives highlighted in red boxes. The numerically determined SHA of Pt (black star) is included for comparison [56].

There are additional materials from this group with larger SHAs than Pt, which strongly suggests their promise in spintronics applications.

Conclusions and perspectives. We systematically investigated the intrinsic spin Hall effect (SHE) in topological semimetallic systems with high Chern numbers, which suggests that SHE enhancement can occur under the energetic alignment of high Chern number Kramers-Weyl points (KWPs). At $\mathcal{C}=4$ KWP alignment, the spin Hall conductivity reveals a characteristic camel-back structure, whose stationary points can be traced to constructive contributions from intense spin Berry curvature hotspots near the high Chern number KWPs and SOC-induced nested bands emanating from these high degeneracy KWPs.

It is important to note that the high Chern numbers in the models studied here are mainly due to high band degeneracies. However, there are gapless systems with high Chern numbers, which are due to higher-order band dispersions [68]. The SHE enhancement mechanism in this work may differ in such systems. For a more complete understanding, systematic studies along these lines are essential.

Acknowledgments. C.O.A., W.J., D.S., S.L., J.P.W., and T.L. were partially supported by the SMART, one of seven centers of nCORE, a Semi-conductor Research Corporation program, sponsored by the National Institute of Standards and Technology (NIST). C.O.A., D.S., J.P.W., and T.L. also acknowledge partial support from the DARPA ERI FRANC program under HR001117S0056-FP-042. S.L. and T.L.

acknowledge partial support by the National Science Foundation through the University of Minnesota MRSEC under Award No. DMR-2011401. S.L. is also supported by the Basic

Science Research Program through the National Research Foundation of Korea funded by the Ministry of Education (NRF-2021R1A6A3A14038837).

- [1] A. Aronov and G. Pikus, Spin injection into semiconductors, Sov. Phys. Semicond. **10**, 698 (1976).
- [2] S. Datta and B. Das, Electronic analog of the electro-optic modulator, Appl. Phys. Lett. 56, 665 (1990).
- [3] M. Dyakonov and V. Perel, Current-induced spin orientation of electrons in semiconductors, Phys. Lett. A **35**, 459 (1971).
- [4] J. E. Hirsch, Spin Hall effect, Phys. Rev. Lett. 83, 1834 (1999).
- [5] M. W. J. Prins, H. van Kempen, H. van Leuken, R. A. de Groot, W. V. Roy, and J. D. Boeck, Spin-dependent transport in metal/semiconductor tunnel junctions, J. Phys.: Condens. Matter 7, 9447 (1995).
- [6] K. Uchida, S. Takahashi, K. Harii, J. Ieda, W. Koshibae, K. Ando, S. Maekawa, and E. Saitoh, Observation of the spin Seebeck effect, Nature (London) 455, 778 (2008).
- [7] G. E. W. Bauer, E. Saitoh, and B. J. van Wees, Spin caloritronics, Nat. Mater. 11, 391 (2012).
- [8] S. Seki, T. Ideue, M. Kubota, Y. Kozuka, R. Takagi, M. Nakamura, Y. Kaneko, M. Kawasaki, and Y. Tokura, Thermal generation of spin current in an antiferromagnet, Phys. Rev. Lett. 115, 266601 (2015).
- [9] A. Hirohata and K. Takanashi, Future perspectives for spintronic devices, J. Phys. D 47, 193001 (2014).
- [10] Y. Zhang, Q. Xu, K. Koepernik, R. Rezaev, O. Janson, J. Železný, T. Jungwirth, C. Felser, J. van den Brink, and Y. Sun, Different types of spin currents in the comprehensive materials database of nonmagnetic spin Hall effect, npj Comput. Mater. 7, 167 (2021).
- [11] V. P. Amin, J. Li, M. D. Stiles, and P. M. Haney, Intrinsic spin currents in ferromagnets, Phys. Rev. B 99, 220405(R) (2019).
- [12] V. P. Amin, J. Zemen, and M. D. Stiles, Interface-generated spin currents, Phys. Rev. Lett. 121, 136805 (2018).
- [13] D. J. P. de Sousa, M. J. Sammon, R. Kim, H. Li, I. A. Young, and T. Low, Spin torque generated by valley Hall effect in WSe₂, Phys. Rev. B 106, 184412 (2022).
- [14] S.-h. C. Baek, V. P. Amin, Y.-W. Oh, G. Go, S.-J. Lee, G.-H. Lee, K.-J. Kim, M. D. Stiles, B.-G. Park, and K.-J. Lee, Spin currents and spin-orbit torques in ferromagnetic trilayers, Nat. Mater. 17, 509 (2018).
- [15] J. Sinova, S. O. Valenzuela, J. Wunderlich, C. H. Back, and T. Jungwirth, Spin Hall effects, Rev. Mod. Phys. 87, 1213 (2015).
- [16] A. Davidson, V. P. Amin, W. S. Aljuaid, P. M. Haney, and X. Fan, Perspectives of electrically generated spin currents in ferromagnetic materials, Phys. Lett. A 384, 126228 (2020).
- [17] L. Liu, C.-F. Pai, Y. Li, H. W. Tseng, D. C. Ralph, and R. A. Buhrman, Spin-torque switching with the giant spin Hall effect of tantalum, Science 336, 555 (2012).
- [18] D. MacNeill, G. M. Stiehl, M. H. D. Guimaraes, R. A. Buhrman, J. Park, and D. C. Ralph, Control of spin-orbit torques through crystal symmetry in WTe₂/ferromagnet bilayers, Nat. Phys. 13, 300 (2017).
- [19] S. Shi, J. Li, C.-H. Hsu, K. Lee, Y. Wang, L. Yang, J. Wang, Q. Wang, H. Wu, W. Zhang *et al.*, Observation of the out-of-plane polarized spin current from CVD grown WTe₂, Adv. Quantum Technol. 4, 2100038 (2021).

- [20] F. Xue, C. Rohmann, J. Li, V. Amin, and P. Haney, Unconventional spin-orbit torque in transition metal dichalcogenide-ferromagnet bilayers from first-principles calculations, Phys. Rev. B 102, 014401 (2020).
- [21] S. Murakami, N. Nagaosa, and S.-C. Zhang, Dissipationless quantum spin current at room temperature, Science 301, 1348 (2003).
- [22] S. Murakami, Intrinsic spin Hall effect, in *Advances in Solid State Physics*, edited by B. Kramer (Springer Berlin Heidelberg, Berlin, Heidelberg, 2006), pp. 197–209.
- [23] J. Sinova, D. Culcer, Q. Niu, N. A. Sinitsyn, T. Jungwirth, and A. H. MacDonald, Universal intrinsic spin Hall effect, Phys. Rev. Lett. 92, 126603 (2004).
- [24] D. Culcer, Y. Yao, and Q. Niu, Coherent wave-packet evolution in coupled bands, Phys. Rev. B **72**, 085110 (2005).
- [25] M. Gradhand, D. V. Fedorov, F. Pientka, P. Zahn, I. Mertig, and B. L. Györffy, First-principle calculations of the Berry curvature of Bloch states for charge and spin transport of electrons, J. Phys.: Condens. Matter 24, 213202 (2012).
- [26] D. Xiao, M.-C. Chang, and Q. Niu, Berry phase effects on electronic properties, Rev. Mod. Phys. 82, 1959 (2010).
- [27] E. Derunova, Y. Sun, C. Felser, S. S. P. Parkin, B. Yan, and M. N. Ali, Giant intrinsic spin Hall effect in W₃Ta and other A15 superconductors, Sci. Adv. **5**, eaav8575 (2019).
- [28] G. Y. Guo, S. Murakami, T.-W. Chen, and N. Nagaosa, Intrinsic spin Hall effect in platinum: First-principles calculations, Phys. Rev. Lett. 100, 096401 (2008).
- [29] B. B. Prasad and G.-Y. Guo, Tunable spin Hall and spin Nernst effects in Dirac line-node semimetals XCuYAs (X = Zr, Hf; Y = Si,Ge), Phys. Rev. Mater. 4, 124205 (2020).
- [30] Y.-F. Zhao, R. Zhang, R. Mei, L.-J. Zhou, H. Yi, Y.-Q. Zhang, J. Yu, R. Xiao, K. Wang, N. Samarth *et al.*, Tuning the Chern number in quantum anomalous Hall insulators, Nature (London) 588, 419 (2020).
- [31] C. Fang, M. J. Gilbert, and B. A. Bernevig, Large-Chernnumber quantum anomalous Hall effect in thin-film topological crystalline insulators, Phys. Rev. Lett. **112**, 046801 (2014).
- [32] H. Li, C.-Z. Chen, H. Jiang, and X. C. Xie, Coexistence of quantum Hall and quantum anomalous Hall phases in disordered MnBi₂Te₄, Phys. Rev. Lett. **127**, 236402 (2021).
- [33] T. M. McCormick, R. C. McKay, and N. Trivedi, Semiclassical theory of anomalous transport in type-II topological Weyl semimetals, Phys. Rev. B 96, 235116 (2017).
- [34] C. Shekhar, Chirality meets topology, Nat. Mater. 17, 953 (2018).
- [35] G. Chang, B. J. Wieder, F. Schindler, D. S. Sanchez, I. Belopolski, S.-M. Huang, B. Singh, D. Wu, T.-R. Chang, T. Neupert *et al.*, Topological quantum properties of chiral crystals, Nat. Mater. 17, 978 (2018).
- [36] N. B. M. Schröter, S. Stolz, K. Manna, F. de Juan, M. G. Vergniory, J. A. Krieger, D. Pei, T. Schmitt, P. Dudin, T. K. Kim *et al.*, Observation and control of maximal Chern numbers in a chiral topological semimetal, Science 369, 179 (2020).
- [37] G. Chang, S.-Y. Xu, B. J. Wieder, D. S. Sanchez, S.-M. Huang, I. Belopolski, T.-R. Chang, S. Zhang, A. Bansil, H. Lin

- et al., Unconventional chiral fermions and large topological Fermi arcs in RhSi, Phys. Rev. Lett. **119**, 206401 (2017).
- [38] D. A. Pshenay-Severin, Y. V. Ivanov, A. A. Burkov, and A. T. Burkov, Band structure and unconventional electronic topology of CoSi, J. Phys.: Condens. Matter 30, 135501 (2018).
- [39] P. Tang, Q. Zhou, and S.-C. Zhang, Multiple types of topological fermions in transition metal silicides, Phys. Rev. Lett. 119, 206402 (2017).
- [40] M. Yao, K. Manna, Q. Yang, A. Fedorov, V. Voroshnin, B. Valentin Schwarze, J. Hornung, S. Chattopadhyay, Z. Sun, S. N. Guin *et al.*, Observation of giant spin-split Fermi-arc with maximal Chern number in the chiral topological semimetal PtGa, Nat. Commun. 11, 2033 (2020).
- [41] G. Gatti, D. Gosálbez-Martínez, S. S. Tsirkin, M. Fanciulli, M. Puppin, S. Polishchuk, S. Moser, L. Testa, E. Martino, S. Roth *et al.*, Radial spin texture of the Weyl fermions in chiral tellurium, Phys. Rev. Lett. **125**, 216402 (2020).
- [42] M. Sakano, M. Hirayama, T. Takahashi, S. Akebi, M. Nakayama, K. Kuroda, K. Taguchi, T. Yoshikawa, K. Miyamoto, T. Okuda *et al.*, Radial spin texture in elemental tellurium with chiral crystal structure, Phys. Rev. Lett. 124, 136404 (2020).
- [43] W.-Y. He, X. Y. Xu, and K. T. Law, Kramers Weyl semimetals as quantum solenoids and their applications in spin-orbit torque devices, Commun. Phys. 4, 66 (2021).
- [44] K. Tang, Y.-C. Lau, K. Nawa, Z. Wen, Q. Xiang, H. Sukegawa, T. Seki, Y. Miura, K. Takanashi, and S. Mitani, Spin Hall effect in a spin-1 chiral semimetal, Phys. Rev. Res. 3, 033101 (2021).
- [45] T.-Y. Hsieh, B. B. Prasad, and G.-Y. Guo, Helicity-tunable spin Hall and spin Nernst effects in unconventional chiral fermion semimetals XY (X = Co, Rh; Y = Si, Ge), Phys. Rev. B **106**, 165102 (2022).
- [46] N. H. D. Khang, Y. Ueda, and P. N. Hai, A conductive topological insulator with large spin Hall effect for ultralow power spin-orbit torque switching, Nat. Mater. 17, 808 (2018).
- [47] Y. Sun, Y. Zhang, C. Felser, and B. Yan, Strong intrinsic spin Hall effect in the TaAs family of Weyl semimetals, Phys. Rev. Lett. 117, 146403 (2016).
- [48] Y. Yen and G.-Y. Guo, Tunable large spin Hall and spin Nernst effects in the Dirac semimetals ZrXY(X = Si, Ge; Y = S, Se, Te), Phys. Rev. B **101**, 064430 (2020).
- [49] W. Hou, J. Liu, X. Zuo, J. Xu, X. Zhang, D. Liu, M. Zhao, Z.-G. Zhu, H.-G. Luo, and W. Zhao, Prediction of crossing nodal-lines and large intrinsic spin Hall conductivity in topological Dirac semimetal Ta₃As family, npj Comput. Mater. 7, 37 (2021).
- [50] B. Bradlyn, J. Cano, Z. Wang, M. G. Vergniory, C. Felser, R. J. Cava, and B. A. Bernevig, Beyond Dirac and Weyl fermions: Unconventional quasiparticles in conventional crystals, Science 353, aaf5037 (2016).
- [51] Z. Zhang, G.-B. Liu, Z.-M. Yu, S. A. Yang, and Y. Yao, Encyclopedia of emergent particles in type-IV magnetic space groups, Phys. Rev. B **105**, 104426 (2022).
- [52] Q. Xie, W. Lin, S. Sarkar, X. Shu, S. Chen, L. Liu, T. Zhao, C. Zhou, H. Wang, J. Zhou *et al.*, Field-free magnetization switching induced by the unconventional spinâorbit torque from WTe₂, APL Mater. 9, 051114 (2021).
- [53] D. J. P. de Sousa, P. M. Haney, J. P. Wang, and T. Low, Field-free-switching state diagram of perpendic-

- ular magnetization subjected to conventional and unconventional spin-orbit torques, Phys. Rev. Appl. **18**, 054020 (2022).
- [54] A. Sebastian, M. Le Gallo, R. Khaddam-Aljameh, and E. Eleftheriou, Memory devices and applications for in-memory computing, Nat. Nanotechnol. 15, 529 (2020).
- [55] W. Zhang, B. Gao, J. Tang, P. Yao, S. Yu, M.-F. Chang, H.-J. Yoo, H. Qian, and H. Wu, Neuro-inspired computing chips, Nature Electronics 3, 371 (2020).
- [56] See Supplemental Materials at http://link.aps.org/supplemental/ 10.1103/PhysRevB.108.L201404 for C = 1 4 models; correlations between SHC, SHA, and Chern number; SG-198 tight-binding model; data mining and statistical analysis; computational methods; strain engineering; and SG-198 SHC database. The Supplemental Material also contains Refs. [10,35,37,51,58,62–67].
- [57] G. Y. Guo, Y. Yao, and Q. Niu, *Ab initio* calculation of the intrinsic spin Hall effect in semiconductors, Phys. Rev. Lett. 94, 226601 (2005).
- [58] W. Jiang, D. J. P. de Sousa, J.-P. Wang, and T. Low, Giant anomalous Hall effect due to double-degenerate quasiflat bands, Phys. Rev. Lett. **126**, 106601 (2021).
- [59] Y. Shen, Y. Jin, Y. Ge, M. Chen, and Z. Zhu, Chiral topological metals with multiple types of quasiparticle fermions and large spin Hall effect in the SrGePt family materials, Phys. Rev. B 108, 035428 (2023).
- [60] T. Zhang, Y. Jiang, Z. Song, H. Huang, Y. He, Z. Fang, H. Weng, and C. Fang, Catalogue of topological electronic materials, Nature (London) **566**, 475 (2019).
- [61] L. Wu, F. Tang, and X. Wan, Symmetry-enforced band nodes in 230 space groups, Phys. Rev. B 104, 045107 (2021).
- [62] P. Giannozzi, S. Baroni, N. Bonini, M. Calandra, R. Car, C. Cavazzoni, D. Ceresoli, G. L. Chiarotti, M. Cococcioni, I. Dabo et al., QUANTUM ESPRESSO: A modular and open-source software project for quantum simulations of materials, J. Phys.: Condens. Matter 21, 395502 (2009).
- [63] P. Giannozzi, O. Andreussi, T. Brumme, O. Bunau, M. B. Nardelli, M. Calandra, R. Car, C. Cavazzoni, D. Ceresoli, M. Cococcioni *et al.*, Advanced capabilities for materials modelling with QUANTUM ESPRESSO, J. Phys.: Condens. Matter 29, 465901 (2017).
- [64] A. A. Mostofi, J. R. Yates, G. Pizzi, Y.-S. Lee, I. Souza, D. Vanderbilt, and N. Marzari, An updated version of wannier90: A tool for obtaining maximally-localised Wannier functions, Comput. Phys. Commun. 185, 2309 (2014).
- [65] G. Pizzi, V. Vitale, R. Arita, S. Blügel, F. Freimuth, G. Géranton, M. Gibertini, D. Gresch, C. Johnson, T. Koretsune et al., Wannier90 as a community code: New features and applications, J. Phys.: Condens. Matter 32, 165902 (2020).
- [66] I. Souza, N. Marzari, and D. Vanderbilt, Maximally localized Wannier functions for entangled energy bands, Phys. Rev. B 65, 035109 (2001).
- [67] J. Qiao, J. Zhou, Z. Yuan, and W. Zhao, Calculation of intrinsic spin Hall conductivity by Wannier interpolation, Phys. Rev. B 98, 214402 (2018).
- [68] C. Fang, M. J. Gilbert, X. Dai, and B. A. Bernevig, Multi-Weyl topological semimetals stabilized by point group symmetry, Phys. Rev. Lett. 108, 266802 (2012).